DISCLAIMER

Annual Progress Report
Deformation mechanisms of nanotwinned Al and binary Al alloys

Applicant/Institution: Purdue University
Street Address/City/State/Zip: 155 South Grant Street, West Lafayette, IN, 47907-2114
Postal Address: 701 W. Stadium Ave. West Lafayette IN 47907-2045
Principal Investigator: Xinghang Zhang,
Address: 701 W. Stadium Ave., West Lafayette IN 47907-2045
Telephone Number: 765-494-4100
Email: xzhang98@purdue.edu
Co-PI: Jian Wang, University of Nebraska, Lincoln
Administrative Point of Contact name, telephone number, email:
Susan Corwin, Tel: 765-494-6204, Email: coepreaward@purdue.edu
Funding Opportunity Announcement Number: DE-FOA-0001414
DOE/Office of Science Program Office: Office of Basic Energy Science, Materials Science and
Engineering Division
Topic Area: Mechanical behavior and radiation effects
DOE/Office of Science Program Manager Contact: Dr. John Vetrano, 301-903-5976, john.vetrano@science.doe.gov
Date of the report and period covered by the report: **09/1/2021-08/31/2024**
DOE Award number: DE-SC0016337

I. Overview and major accomplishments

I.1. Overview and major scientific hypotheses.

The objective of this proposal is to investigate, at a fundamental level, the deformation mechanisms of **nanotwinned (NT)** Al alloys with high density **twin boundaries (TBs)** and **stacking faults (SFs)**. Nanotwinned metals with low **stacking fault energy (SFE)**, such as Cu and Ag, have shown outstanding strength and tensile ductility. Twin boundaries play a critical role to enhance the strength and work hardening ability of these metals and alloys, and thus lead to significant plasticity. Al alloys have ultra-high stacking fault energy, and thus are often considered to be nearly free from growth twins and SFs. However, our recent studies show that a significant number of nanotwins and 9R phase can be introduced in Al and certain Al alloys, and lead to high flow stresses. In this project we will test the following hypotheses:

1) A comprehensive view of the energetics of solutes on defect formation energy, rather than intrinsic stacking fault energy alone, is necessary to evaluate the influence of solute on the formation of growth twins and 9R in Al alloys. In our previous project, we have hypothesized that NT Al alloys form because certain solutes can reduce the intrinsic SFE of Al. Our recent microscopy studies show that Fe, Co and Ni, can significantly promote the formation of growth twins in Al. DFT calculations show that solute, such as Fe, Co and Ni, increases the SFE of Al.

Hence the intrinsic SFE alone is insufficient to predict the formation of growth twins in Al alloys. We hypothesize that, to understand the formation of growth twins and 9R, it is necessary to develop a comprehensive view of solute modified energetics, including stable and unstable SFE, and the energetics for formation of point defects and the influence of solutes on diffusivity of matrix atoms.
2) Nanotwinned Al alloys may have unique deformation mechanisms. Prior MD simulations have suggested that metals with high stacking fault energy, such as Al, would have low work hardening ability. However, NT metals, such as Cu and Ag have shown simultaneous enhancement of strength and ductility. Furthermore our compression tests show that NT Al-Fe alloys have high compressive strength and work hardening ability. We thus hypothesize that 9R phase and SFs may introduce work hardening ability and improve strain rate sensitivity in general in various NT Al alloys and some of these NT Al alloys may also have outstanding tensile strength and ductility.
3) The strength of NT Al alloys may be determined by the critical stress for migration of 9R phase. We hypothesize that the critical stress for migration of 9R phase may depend on the energetics of solutes and TBs in each alloy. Furthermore, we hypothesize solutes that stabilize 9R phase in Al may improve their thermal stability and high-temperature mechanical strength.

I. 2. A brief description of major accomplishments (progress update)

In what follows, we briefly summarize our accomplishment in fundamental understandings on the synthesis, deformation mechanisms and thermal stability of NT Al alloys.

A. Understand the fundamental mechanisms that promote the growth of twins and SFs in Al

Based on our previous findings, we know that several approaches may introduce TBs in Al, including layer interfaces and solutes. Here we show two examples that improve our understandings on the usage of interfaces and solute to introduce twins, and DFT calculations that significantly improve our understandings on the formation of twins and SFs in Al.

A1. Understand the influence of layer interface on introduction of SFs in Al.

(S. Xue, Y. Zhang, Q. Li, J. Ding, H. Wang and X. Zhang, Tailoring the formation of twins in Al by introducing epitaxial layer interfaces, **Scripta Materialia,** 192 (2021), 1-6.)

In 2013, we have shown that coherent Ag/Al layer interface is instrumental to the formation of growth twins in Al. The twins and stacking faults (SFs) in Ag seed layers were "replicated" in Al through coherent Ag/Al layer interface. Based on this understanding, we hypothesize that 1) incoherent layer interfaces may not promote the formation of growth twins in Al/X multilayers and 2) if the X layer does not twin easily, then we are less likely to observed growth twins in Al.

We have performed an additional study and found that this hypothesis is partially correct. As interfaces between Al and Mg should be incoherent and Mg does not form twins easily, and one would not anticipate the growth twins or SFs in Al. Yet we found abundant growth twins, SFs in Al in Al/Mg nanolayers.

In this paper, coherent twin boundaries (CTBs), incoherent twin boundaries (ITBs), and 9R phase were introduced into epitaxial layers of Al grown on Si(111) using heterogeneous

epitaxial Mg layers. Typically, uninterrupted growth of Al films on Si(111) leads to coarse grains with little to no TBs, as shown in Fig. 7a-c. In the incoherent Al/Co nanolayers in Fig. 7d-f, we did not observe TBs or SFs in Al. However, when using a thin Mg layer to interrupt the growth of the Al film periodically (Fig. 7g-I), the coherent Al/Mg layer interfaces form and the interfaces allow for the continued growth of CTBs, ITBs, and a significant fraction of 9R phase to form in the films by maintaining the strong (111) texture. This study demonstrates an effective method for introducing a high density of twins into a high SFE metal such as Al.

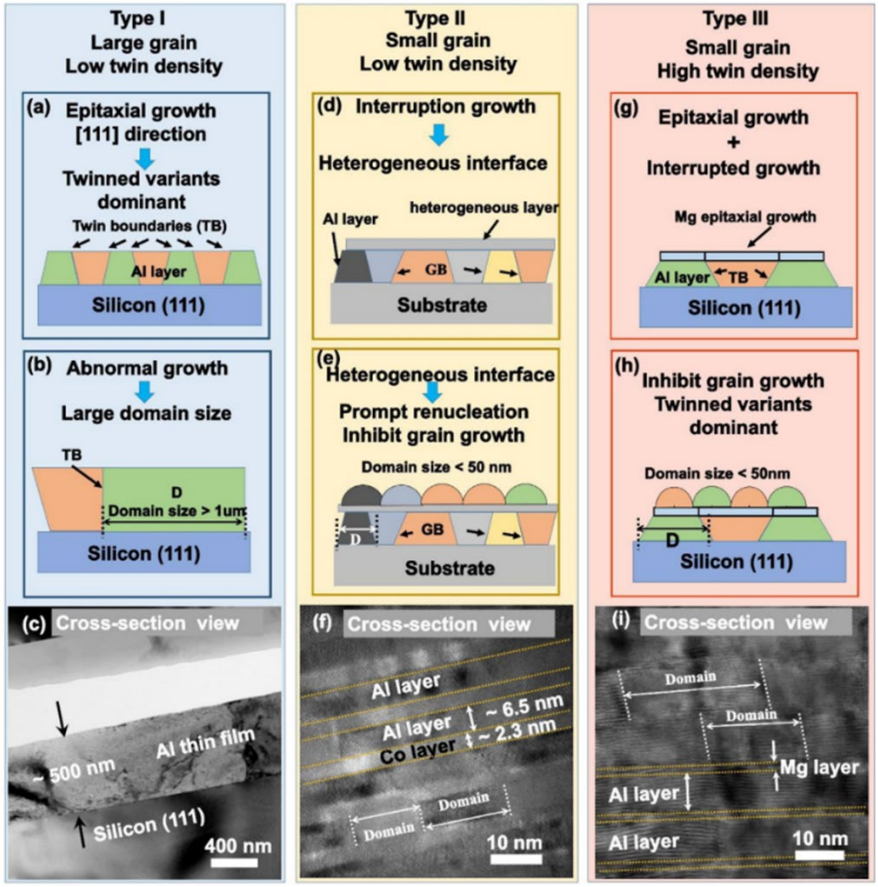

Figure 1. Schematics of three types of scenarios for the twin formation mechanisms in high SFE metals. (a,b) Type I: single layer epitaxy with few TBs. Twin variants nucleate when Al grows epitaxially on Si (111) substrate, and abnormal grain growth eliminates most of the TBs. (c) A XTEM micrograph showing the Type I scenario: epitaxial Al with large grain and few TBs. (d,e) Type II: incoherent layer interface leads to smaller grains but few TBs. (f) A XTEM micrograph showing the lack of TBs in incoherent Al6.5 nm/Co2.3 nm multilayers. (g,h) Type III: small grain and high-density TBs. Thin Mg layers can grow epitaxially on (111) Al layers to maintain the epitaxial growth of the film, promoting grain refinement in Al layers. (i) A TEM micrograph showing small grain sizes with high-density twins.

A2. The influence of solutes on formation of growth twins in Al.

<u>Microstructural evolution of nanotwinned Al-Zr alloy with significant 9R phase</u>

(Nicholas Richter, Graduate Student, Materials Research Letters, 9(2), 2021)

Fig. 2 shows the potential of various solutes on the formation of SFs in Al. Star indicates that twins and SFs have been formed during sputtering deposition of Al. Question marks represent the systems of interest in this proposal. Bar-circle indicates that growth twins were not observed in co-sputtered Al alloy films.

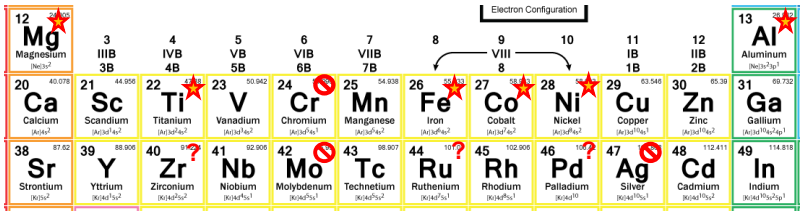

Figure 2. A selected section of periodic table showing electronic configuration of Al and transition metals. The solutes that have enable the formation of twins are marked with stars, and those without twins are labeled with red circles. Elements with question marks will be used as solutes for co-sputtering with Al (binary alloys) to examine their twinnability.

Our previous studies show that Ti can promote the formation of growth twins in Al. Zr is in the same chemical group with Ti, and hence it is natural to speculate that Zr may also promote growth twins in Al. In this work, we fabricated sputtered Al-Zr alloys that possess a fine columnar structure composed of ITBs and abundant 9R phase. These microstructural features, coupled with the high solid solubility, lead to outstanding mechanical strengths (a high hardness reaching 4.2 GPa). DFT calculations reveal that the addition of Zr reduces the SFE of the Al alloy, and the detwinning energy barrier has been increased substantially, attributing to the formation of high twin density and broad 9R phase. Analyses show that ITBs as well as 9R phase play a critical role on the strengthening of NT Al alloys.

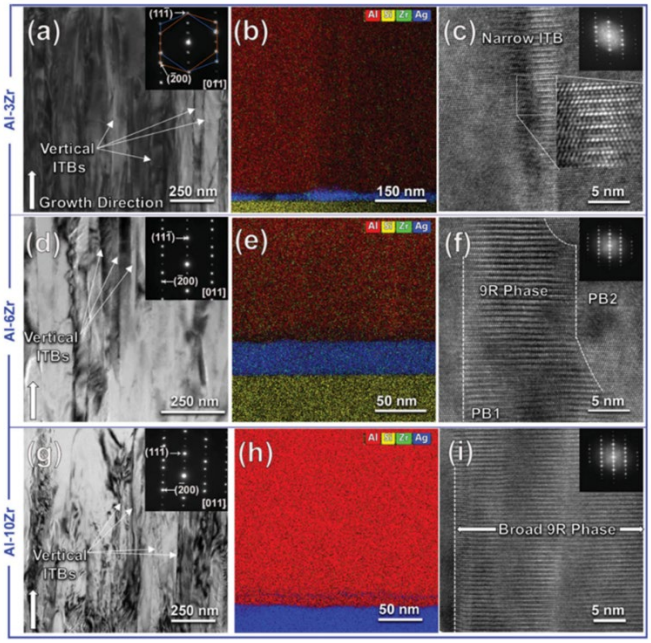

Figure 3. Cross-section TEM (XTEM) micrographs of NT Al-Zr alloy films. (a,d,g) Bright-field (BF) XTEM image with inserted SAD pattern showing columnar grains bounded by ITBs. Columnar refinement occurs at higher Zr content. (b,e,h) EDS maps showing complete solid solution at all compositions. (c,f,h) High-resolution TEM (HRTEM) images of (c) narrow ITB, (f) extended ITB, forming 9R phase, and (i) broad 9R phase, spanning across 40 nm.

The absence of growth twins in sputtered high-strength Al–Cr alloys

(Qiang Li, Graduate Student, International Journal of Plasticity, 137, 2021)

Cr is an interesting element as it is right next to Fe in periodic table, but has significantly different impact on defect formation in Al. For instance, we did not observe any growth twins in Al-Cr films. Here, we systematically investigated the microstructural transition and microstructure-dependent flow stress and plasticity in the sputtered $Al_{100-x}Cr_x$ (x = 0-25 at.%) systems. An unusual multistage FCC - intermetallic - amorphous phase transition was identified, shown in Fig. 4a-g, and Cr segregation facilitated the formation of different phases depending on the alloy compositions, but did not lead to growth twins or SFs in Al.

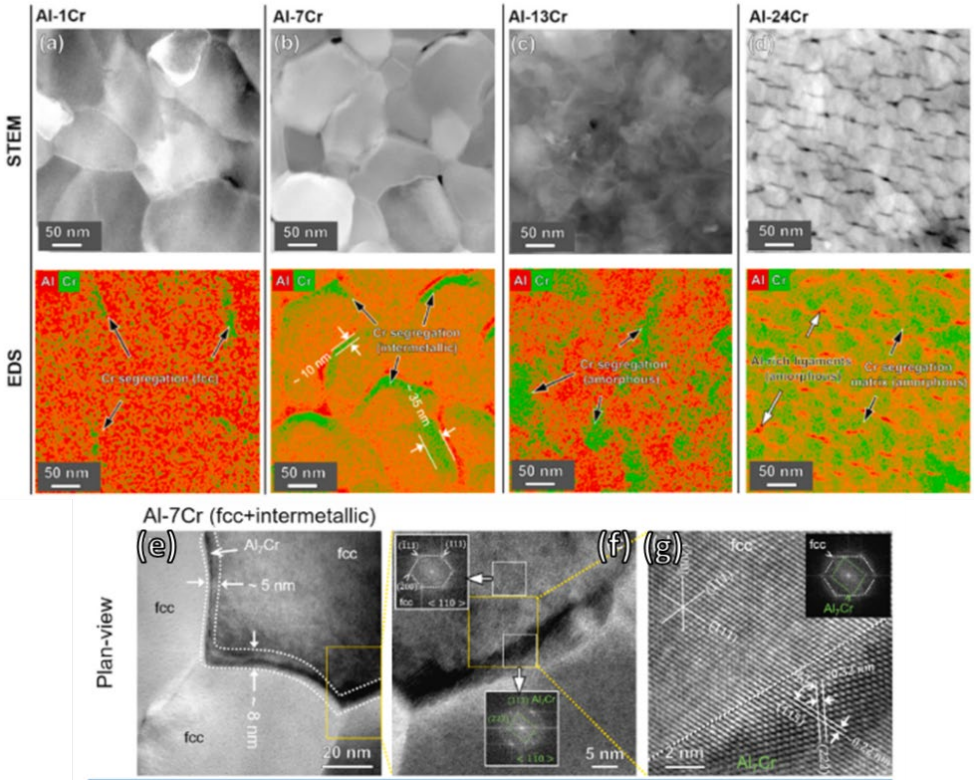

Figure 4. STEM images with the corresponding EDS compositional maps of various Al-Cr films. (a) Minor Cr segregation occurs in Al–1Cr. (b) The Al–7Cr film has prominent Cr segregation along GBs. (c) Al–13Cr has large patches of Cr-enriched regions. (d) The Al–24Cr film consists of Al-rich ligaments separating regions of the Al–Cr amorphous matrix. (e) Plan-view TEM micrograph of Al–7Cr alloy showing FCC grain interiors surrounded by several nm thick GBs. (f,g) HRTEM images showing intermetallic Al7Cr along GBs.

In Al-Fe system, we have discovered the strongest Al alloys to date. However, Al-Cr painted very different pictures. The multiple phases in binary Al-Cr alloys make this an interesting system to explore. We also show that although twin boundaries are not introduced in binary Al-Cr systems, 20 at% Cr can boost the mechanical strength to beyond 2.5 GPa, another record for Al alloys. The amorphous nature of such system leads to shear instability, though.

A3. First-principles calculations for understanding the formation of twins in Al alloys
(Mingyu Gong, Post-doctoral Fellow, submitted to Acta Materialia)

While we have explored numerous binary Al alloys with nanotwins and SFs experimentally and computationally, there is a need to compare and understand the influence of these solutes on defect formation in binary Al alloys. Such a fundamental understanding will prompt the discovery of new Al alloys with unprecedented properties and unique microstructures.

In this work, we used first-principles density-functional theory (DFT) calculations to study the role of eleven solutes in modifying microstructures and enhancing mechanical properties of sputtered Al alloys. The calculated extra binding energies associated with impurity elements are shown in Fig. 5a. The sequence of elements follows number of unfilled electrons. Among 11 impurity elements, Fe, Co and Ni impurities, next to each other on the same row of periodic table, provide the largest extra binding energy, and thus largely reduce the diffusivity of Al adatoms and clusters on {111} surfaces, decreasing columnar grain size. The extra binding energy associated with Mg, Si, Zr, Ru and Pd impurities is smaller than that associated with Fe, Co and Ni impurities, indicating relatively weak trapping effect.

Fig. 5b shows the generalized SFEs in pure Al (black curve) and Al-6.25 at.% Fe (red curve). The intrinsic SFE (ISFE) of pure Al (140.85 mJ/m^2) and Al-6.25Fe (139.10 mJ/m^2) are close, but the unstable stacking fault energy (USFE) of Al-6.25Fe (199.94 mJ/m^2) is higher than that of pure Al (174.80 mJ/m^2). Consequently, the energy barrier associated with the ISF recovery (which is the difference between USFE and ISFE) of Al-6.25Fe (60.84 mJ/m^2) is higher than that of pure Al (33.95 mJ/m^2). Using the same method, we calculated the SFE profiles with different impurity elements. Fig. 5c shows the variation of the energy barrier associated with ISF recovery with impurity element. Mg, Si, Zn, Pd and Ag do not significantly modify the ISF recovery energy barrier. In contrast, Ti, Fe, Co, Ni, Zr and Ru can increase the energy barrier for SF recovery. Among them, Fe solute has the most significant effect to stabilize SF in Al.

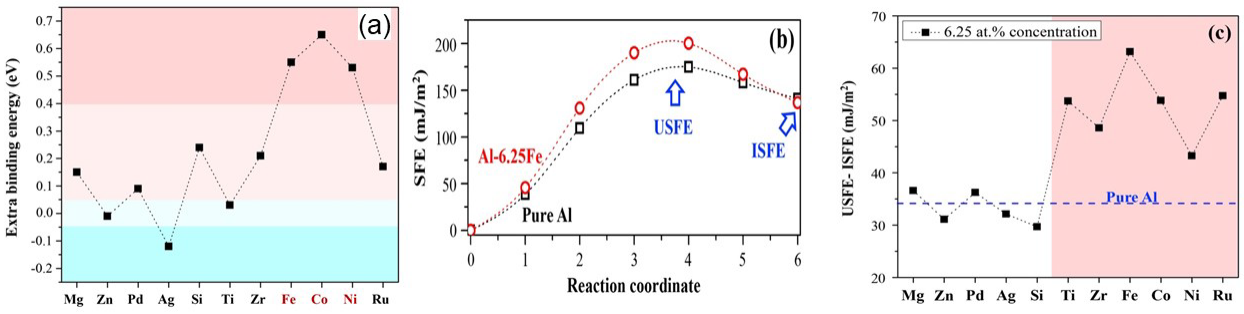

Figure 5. (a) Extra binding energy for an Al adatom due to one impurity atom in the first atomic layer. (b) Variation of generalized SFE in pure Al and Al-6.25Fe on (111) plane. (c) SF recovery barrier (USFE−ISFE) in sputtered Al alloys with 6.25 at.% solute concentration.

A4. Grain boundary and twin boundary solute segregations in nanocrystalline Al-Mg alloy (X.Y. Sheng, Z. Shang, A.Y. Shang, H. Wang, and X. Zhang, Scripta Materialia 245 (2024) 116053)

Chemical segregations at grain boundaries (GBs) have been broadly investigated in Al alloys. However, there are limited experimental evidence demonstrating the dependence of solute segregation on GB characteristics. Here, we quantified solute segregation at GBs in nanocrystalline Al-1Mg (at.%) alloy by combining energy-dispersive X-ray spectroscopy, high-resolution scanning transmission electron microscopy and automated crystallographic indexing and orientation mapping. The dependence of solute segregation on the grain boundary misorientation angle is analyzed. Due to their higher excess free volume, high angle grain boundaries contain more Mg solutes than the low angle grain boundaries. Furthermore, coherent twin boundaries (CTBs) exhibit low solute segregation. However, incoherent twin boundaries (ITBs) display greater solute concentration. The different solute segregation behavior between CTBs and ITBs originates from their grain boundary structure. The solute segregation behavior reported here may shed light on the GB engineering of Al alloys.

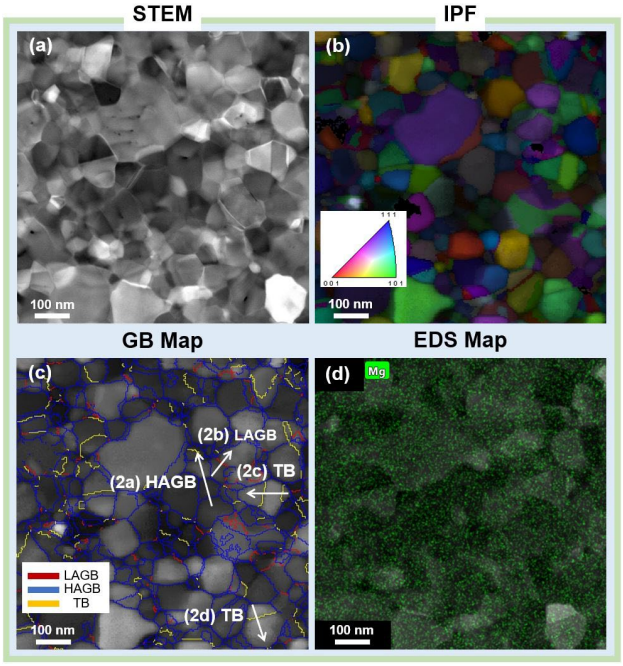

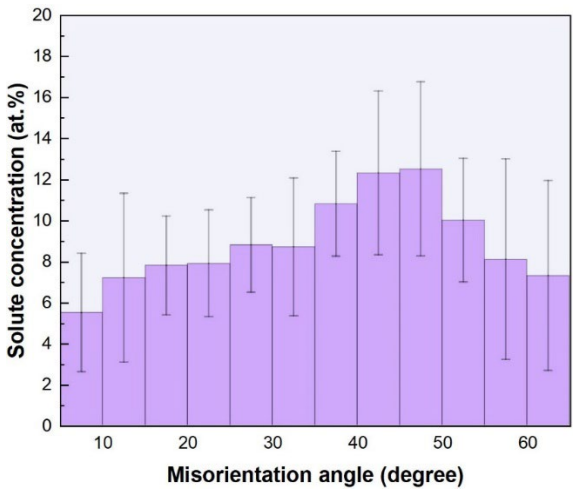

Figure 6 (Left). (a) The HAADF-STEM micrograph of Al-1Mg thin film. (b) The GB map of Al-1Mg taken from the same region overlayed with image quality map. (c) The IPF of Al-1Mg taken from the same region of Fig 1.(a). (d) The corresponding Mg EDS map taken from the same region of Fig 1.(a).

Figure 7 (Right). The concentration of segregated Mg solutes at GBs as a function of GB misorientation angle.

B. Deformation mechanisms of NT Al alloys

B1. Plastic anisotropy and tension-compression asymmetry in NT Al–Fe alloys

(Qiang Li, International Journal of Plasticity, 132, 2020, top 25 downloaded paper)

Our prior study shows that these ultrastrong NT Al-Fe alloys have significant plasticity under compression. What we don't know, however, is if there is anisotropy in deformation behavior of NT Al alloys. In this work, we employed *in-situ* tension and compression tests to inspect the orientation-dependent mechanical response of NT Al-Fe alloys (Fig. 8a). Out-of-plane compression studies (Fig. 8b) reveal significant plasticity and high flow stress of 2 GPa. The high strength arises from the barrier resistance of ITBs, and significant plasticity arises from the capability of ITB migration and subsequent grain coarsening. During in-plane tension tests, we observed in brittle fracture along GBs (Fig. 8c). In comparison, intergranular shear propagation was observed under out-of-plane tension condition with a peak flow stress of 1.8 GPa (Fig. 8d).

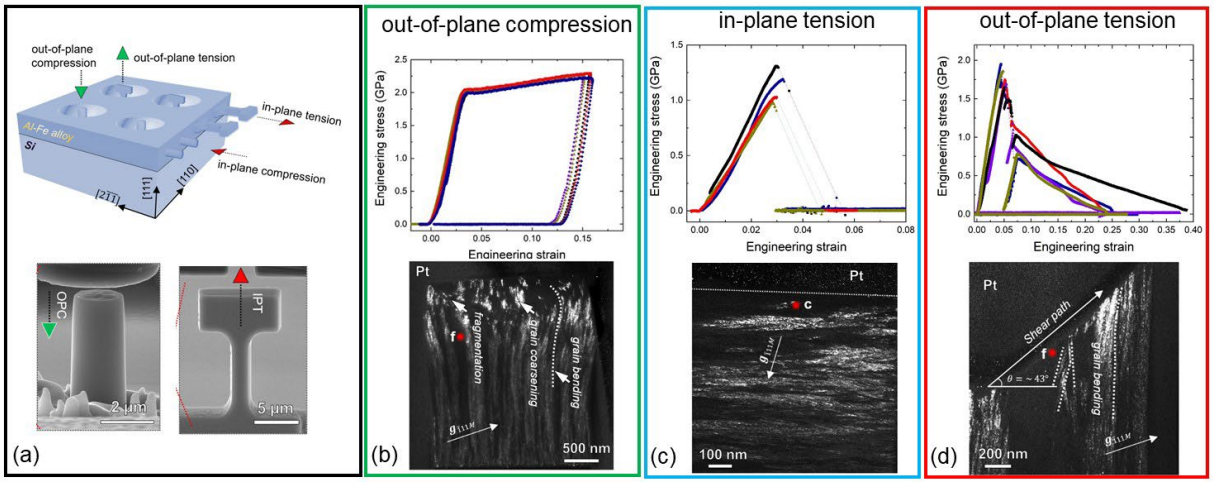

Figure 8. (a) Schematics of nt Al-Fe alloys with highly directional GBs deposited on Si substrate and the compressive and tensile loading directions relative to GB direction. (b) Out-of-plane compression studies reveal significant plasticity and high flow stress, 2GPa. Grain coarsening via migration of ITBs was observed in TEM analysis of deformed pillar. (c) Premature brittle fracture was observed along GBs under in-plane tension condition. (d) Intergranular shear propagation was deflected by GBs under out-of-plane tension condition with a peak flow stress of 1.8 GPa.

In addition to the anisotropic deformation behaviors, the current study also reveals tension-compression asymmetry depending on test directions. For nanocrystalline and ultrafine grained metals with equiaxed grains, σ_y^C/σ_y^T increases from 1 for dislocation-mediated plasticity to ~1.6 for GB-dominated deformation mechanism with decreasing grain sizes as shown in Fig. 9, which is related to the transition from shear-stress dependent to hydrostatic-pressure dependent deformation. The in-plane σ_y^C/σ_y^T ratio of 1.5 for NT Al-Fe with an average grain size of 5 nm appears to be consistent with FCC metals at first. Hence, this observation strongly indicates that the in-plane deformation of Al-Fe with columnar nanograins holds close resemblance to nanocrystalline metals with equiaxed grains and is more in the GB dominated regime. Intriguingly, the out-of-plane σ_y^C/σ_y^T for the same NT Al-Fe is 1.1, similar to ultrafine grained metals where dislocation plasticity dominates. Indeed, TEM studies on specimens tested along out-of-plane

(tension and compression) directions show substantial plasticity and dislocation activities. The implication of such loading direction dependent evolution of stress and compression-tension asymmetry on deformation mechanisms in NT metals with columnar grains may require future MD simulations.

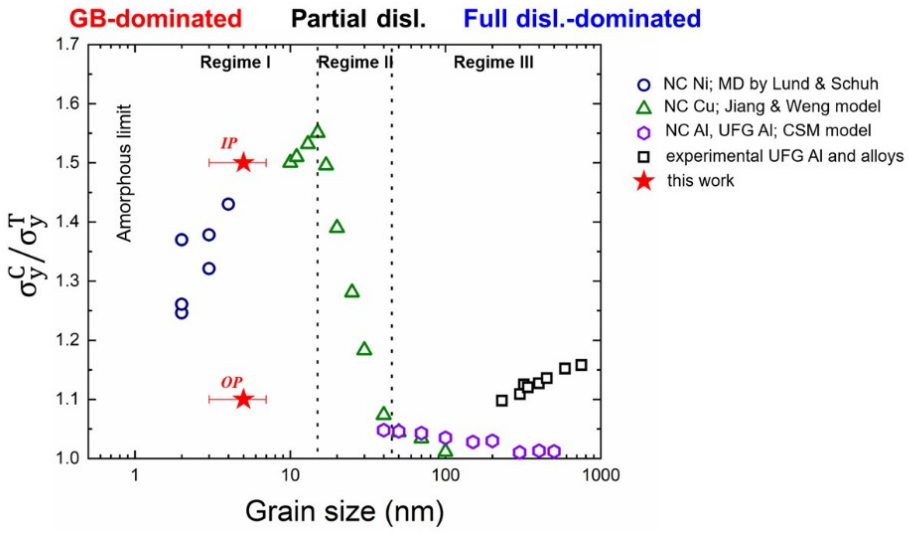

Figure 9. Compression-tension strength asymmetry, σ_y^C/σ_y^T, is plotted for FCC metals across a broad range of grain size. Note that the plot is constructed from literature data using classic models, MD simulation and empirical results. Two dotted boundaries separating three regimes, representing GB-, partial dislocation- and full dislocation-dominated deformation mechanism, respectively. Though not arbitrarily selected, two boundaries are decided approximately and would be influenced by intrinsic parameters of FCC metals. The ratio of σ_y^C/σ_y^T is 1.5 and 1 for testing along in-plane and out-of-plane directions.

B2. Nanoscratch-induced microstructure evolution and gradient nanograin formation in NT Al–Ni alloys (Yifan Zhang, Applied Surface Science, Vol 600, 2022)

Nanoscratch testing revealed that NT Al–Ni alloys exhibit a distinct grain refinement process beneath the scratch surface, driven by the evolution of their unique columnar twin structures. TEM cross-sections (Fig. 10 a-e) show that the deformation zone can be divided into four sublayers: a twin-rich matrix (Zone I), a transitional layer with grain rotation and detwinning (Zone II), a plastically deformed nanograin zone (Zone III), and a near-surface gradient nanograin zone (Zone IV). Columnar grains in Zone I contained abundant incoherent twin boundaries (ITBs) and stacking faults (SFs), which gradually transformed into high-angle grain boundaries (HAGBs) in Zones II–IV due to severe plastic deformation. This transition was mediated by collective glide of Shockley partials, detwinning of 9R phases, and grain rotation, as confirmed by HRTEM and ASTAR orientation maps (Fig. 11 a–f). As a result, the original nanotwinned structure evolved into equiaxed nanograins with a clear size gradient as a function of depth, peaking near the middle of the scratch-affected zone.

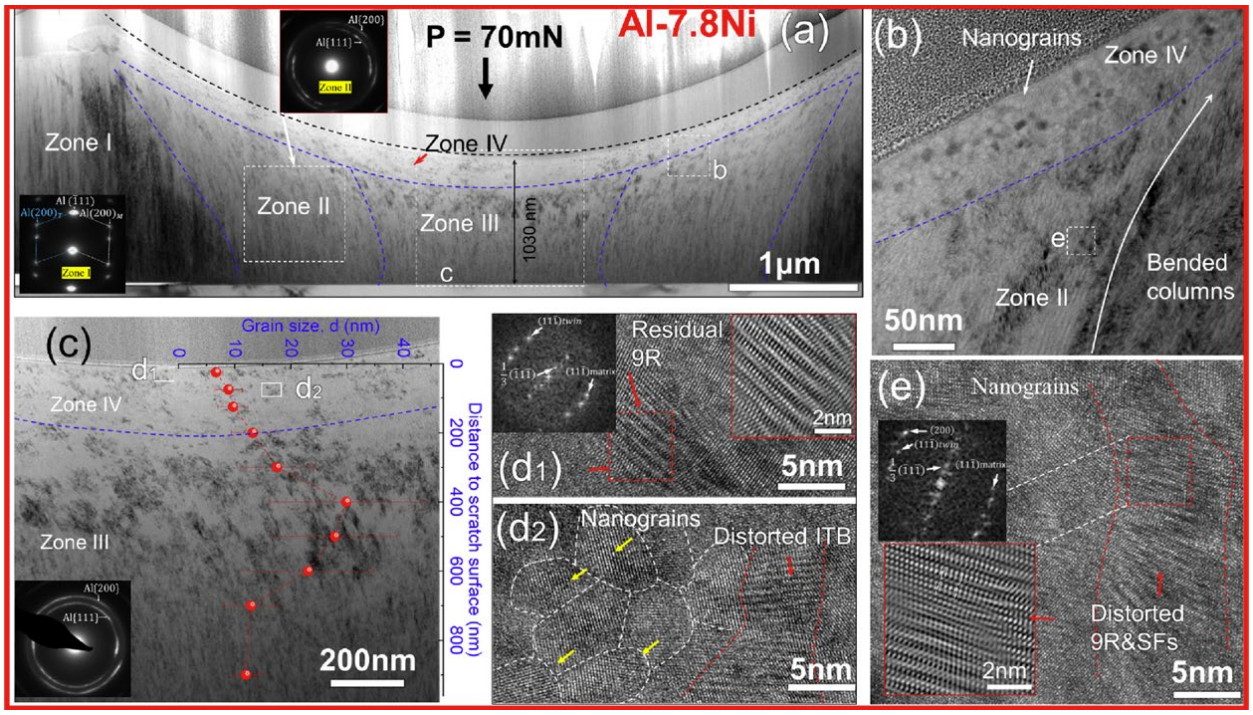

Fig. 10 (a) XTEM image of Al–7.8Ni scratch site. (b) TEM image showing bent columns in Zone II and nanograins in Zone IV. (c) Grain size distribution beneath the indenter. (d1-d2) HRTEM showing nanograins and distorted ITBs in Zone IV. (e) FFT-assisted HRTEM revealing detwinning and 9R-to-nanograin transformation in Zone II.

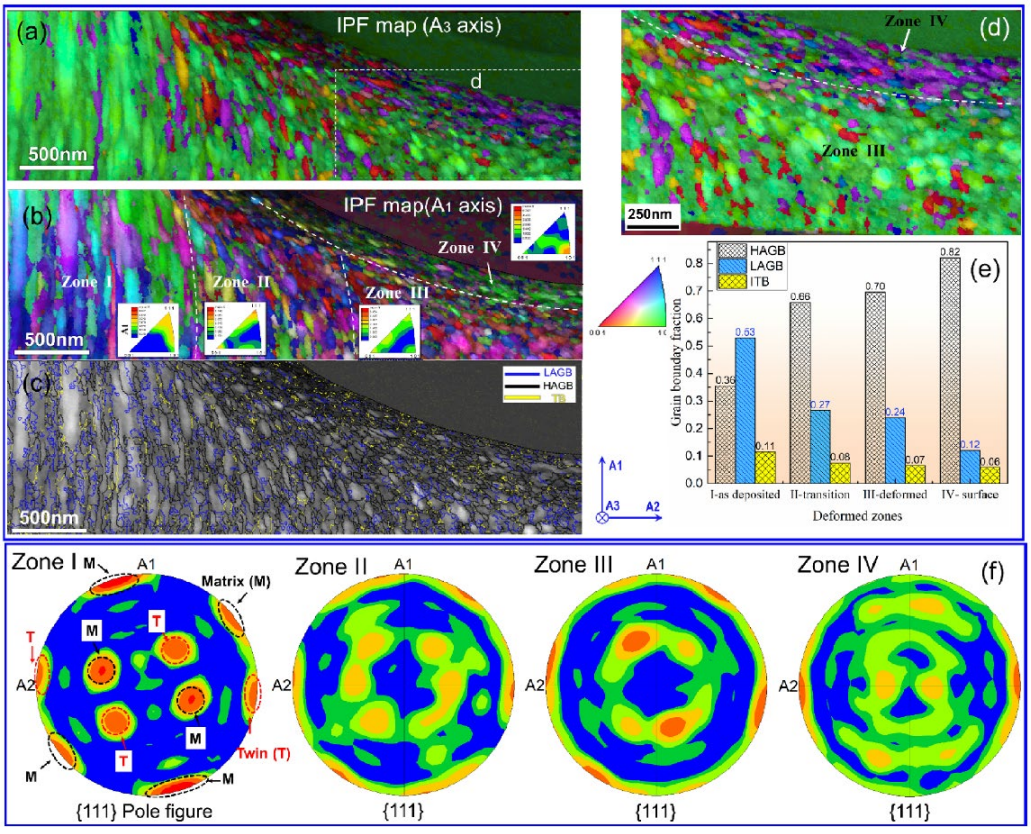

Fig. 11 (a-b) IPF maps of Al–7.8Ni scratch site under 70 mN load. (c) IQ map showing HAGBs and ITBs with varied morphologies. (d) Fraction of HAGBs, LAGBs, and ITBs across Zones I–IV. (e) {111} pole figures from different zones.

The gradient nanograin structure formed in NT Al-Ni alloys is fundamentally different from the dislocation wall dominated microstructure in Al 7075, which lacks significant grain refinement even at high loads (Fig. 12 a-c). The progressive transformation from nanotwinned columns to nanograins was accompanied by a reduction in twin boundary (ITB) density and a corresponding increase in HAGBs. Notably, ASTAR pole figures indicate the loss of twin diffraction spots in the most deformed regions, further validating the detwinning process. The ability of NT Al-Ni alloys to undergo such microstructural evolution under scratch deformation contributes to their enhanced plastic accommodation and wear resistance. This gradient nanograin formation mechanism is a hallmark of discontinuous dynamic recrystallization, enabled by high densities of ITBs and SFs that serve as nucleation sites for new grains.

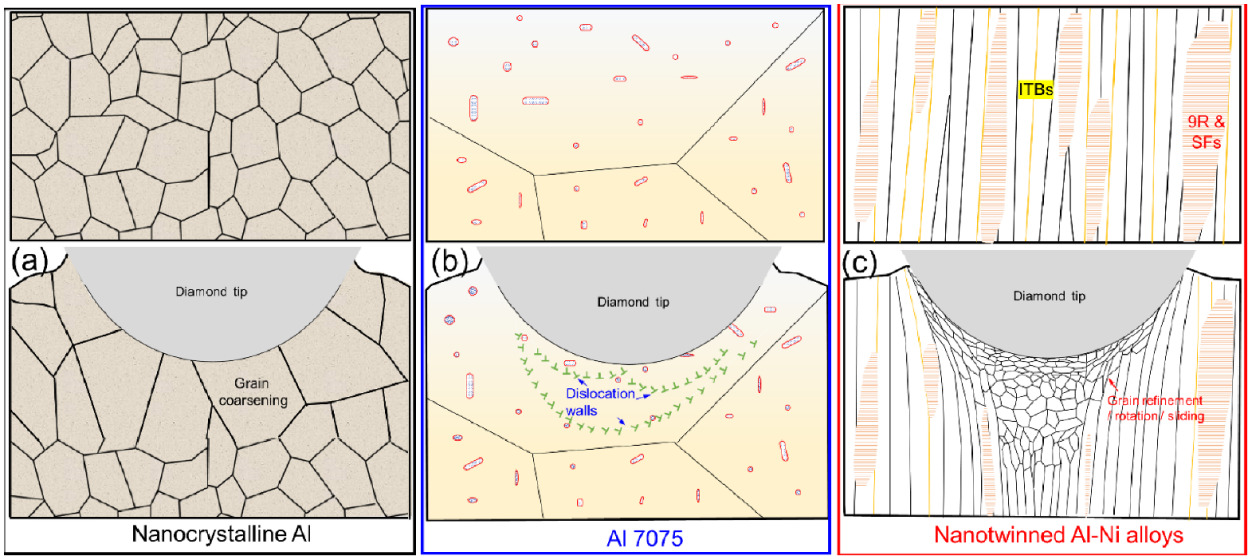

Fig. 12. (ac) Schematics of microstructure evolution in NC Al, Al 7075, and NT Al–Ni alloys during low-speed nanoscratch.

B3. Ultra-high Strength, Deformable Nanocrystalline Al-Pd Alloys

X.Y. Sheng, Z.X. Shang, Y.F. Zhang, K. Xu, N.A. Richter, A.Y. Shang, H. Wang, and X. Zhang, International Journal of Plasticity 189 (2025) 104330.

Strengthening of aluminum (Al) alloys is commonly achieved through precipitation by ageing. However, achieving well dispersed fine precipitates requires a meticulous heat treatment schedule. Here we report sputter-deposited nanocrystalline Al-Pd alloy with nanolaminates, mimicking the structure of vertically aligned nanocomposite (VAN). The nanolaminate consists of alternating Al-Pd solid solution and Al_4Pd intermetallic phase. The periodic composition fluctuation suggests the occurrence of spinodal decomposition. The Al-12.4Pd alloy exhibits a high flow stress of 2.2 GPa with significant work hardening ability, as evidenced by *in situ*

micropillar compression tests performed in a scanning electron microscope. The unique VAN structure induced strengthening and deformation mechanisms are discussed. This study offers a fresh perspective for the design of high-strength deformable Al alloys.

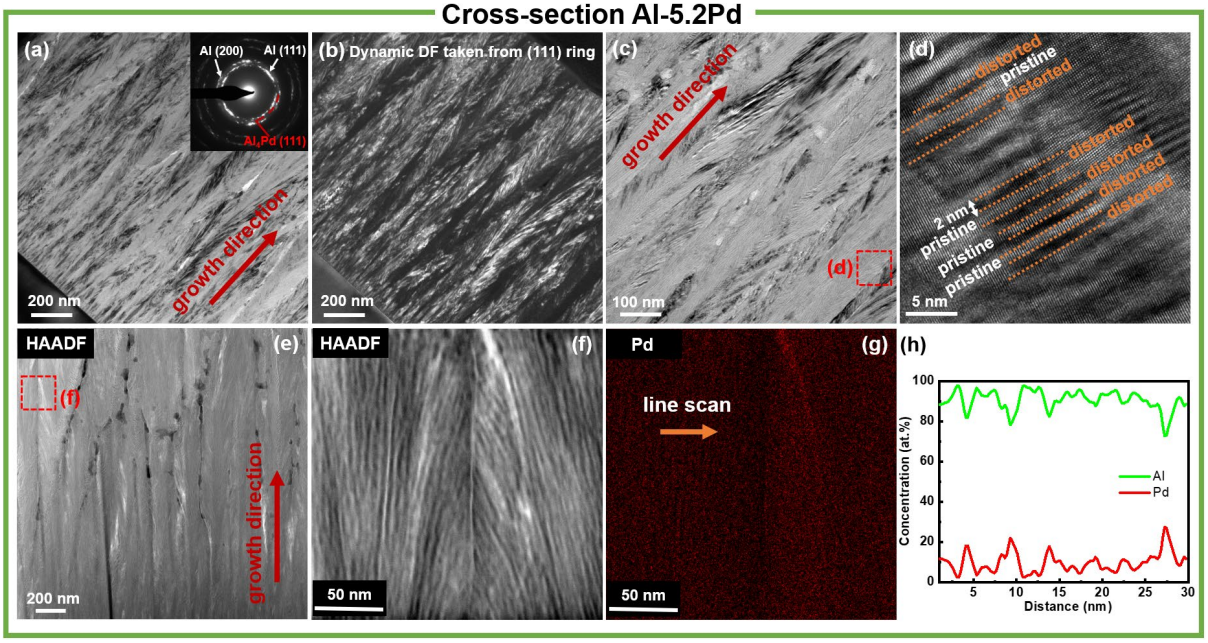

Figure 13. The XTEM micrographs and EDS analysis of the Al-5.2Pd specimen. (a, b) The BF and DF images revealing the columnar nanograins. (c) The magnified BF TEM micrograph showing nanolaminates. (d) HRTEM image revealing the alternating pristine-distorted nanolaminate structure. (e-g) The HAADF-STEM images and the corresponding EDS map showing the periodic segregation of Pd in nanolaminate structure. (h) The EDS line scan profile from the orange line in (g) confirming periodic Pd segregation.

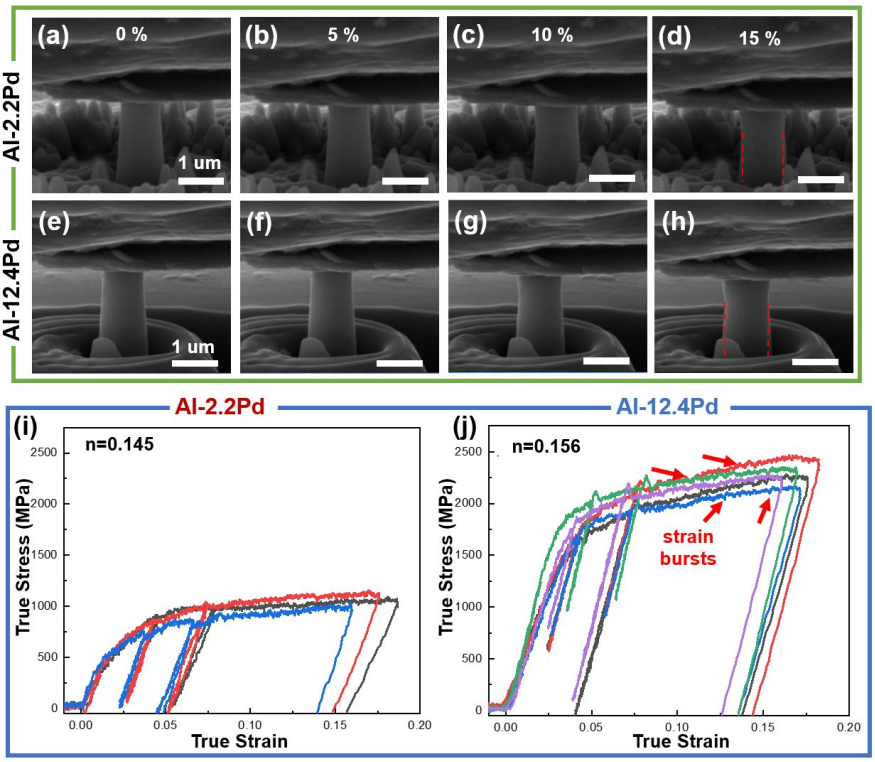

Figure 14. The *in situ* micropillar compression test results of Al-2.2Pd and Al-12.4Pd alloys. (a-d) SEM snapshots captured at different strains during the *in situ* tests of Al-2.2Pd specimens, showing slight bulging of pillar top after compression (Supplementary Video 1). (e-h) SEM snapshots captured during *in situ* tests of Al-12.4Pd. No shear bands were generated during testing, instead the pillar top underwent substantial bulging (Supplementary Video 2). (i, j) The true stress-strain curves of Al-2.2Pd and Al-12.4Pd specimens revealing a flow stress of 1 and 2.2 GPa at a true strain of 5-7%. (n value displayed here is the work hardening exponent.)

C. Thermal stability and high temperature mechanical strength NT Al alloys

C1. Coupled solute effects enable high-temperature strength in NT Al-Fe-Ti alloys

(Qiang Li, Graduate Student, Acta Materialia, 200, 2020)

Al alloys typically soften at 200-300°C or so, hence Al alloys are rarely used above 300°C. Although nanocrystalline Al alloys can significantly strength Al alloys, the nanograins coarsen dramatically beyond 200 °C. In this story, we discovered that a small amount of Ti addition (< 5.0 at.%) to NT Al-Fe alloys can improve the thermal stability remarkably to 400°C. What is more surprising is that these NT Al-Fe-Ti alloys were able to retain ultra-high mechanical strength (> 1.5 GPa) up to 300°C. Such performance established a new record for Al alloys. Even at 400°C, our Al alloys still have mechanical strength of 200 MPa or so. A patent has been filed in conjunction with the Acta Mater publication. This study prompts us to perform more in-depth studies on the influence of multiple solutes on thermal stability of ternary or quaternary Al alloys, so called "**solute synergy**" effects.

TEM micrographs and EDS composition maps (Fig. 15a-b) show the temperature-dependent microstructure and chemical evolutions of NT Al-Fe and NT Al-Fe-Ti alloys. Both as-deposited alloys contain super-saturated solutes and ultra-fine columnar nanotwins. During annealing, solute supersaturation and nanotwins are retained up to 280 °C for NT $Al_{94.5}Fe_{5.5}$ alloys and up to 350 °C for nt $Al_{89.5}Fe_{5.5}Ti_{4.7}$ alloys. Solute segregation, precipitation and recrystallization take place at higher temperatures. Correspondingly, as shown in Fig. 15c, $Al_{89.5}Fe_{5.5}Ti_{4.7}$ alloys retain high strength at 300 °C while $Al_{94.5}Fe_{5.5}$ alloy does not. Fe solutes act as effective grain refiner, forming super-strong alloys. Meanwhile, Ti solutes as structural stabilizer form strong Fe-Ti pairs, thus enhancing solute segregation at ITBs, delaying Fe agglomeration and preventing grain coarsening.

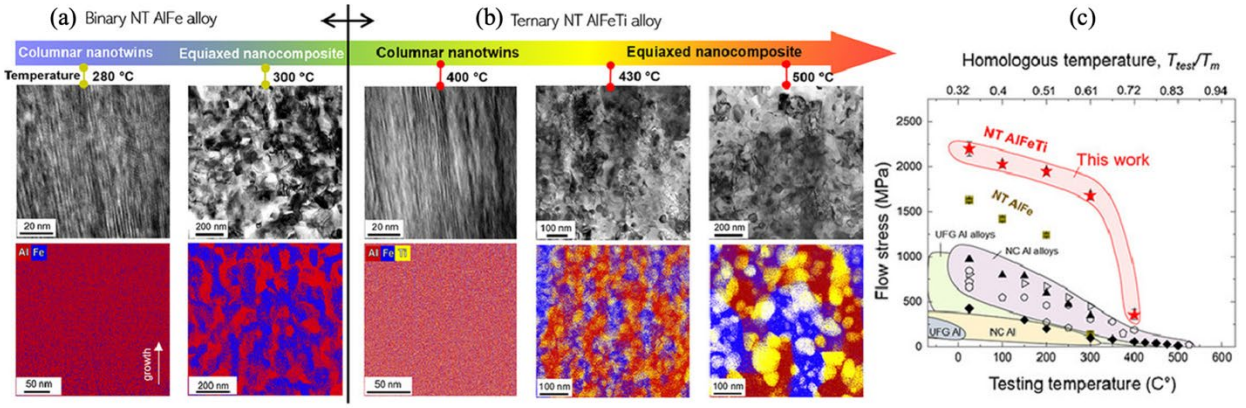

Figure 15. A temperature-dependent microstructure and chemical evolutions revealing (a) NT $Al_{94.5}Fe_{5.5}$ retained solute supersaturation and nanotwins up to 280 ℃, and underwent a concurrent precipitation and recrystallization at 300 ℃. (b) NT $Al_{89.5}Fe_{5.5}Ti_{4.7}$ remained columnar nanotwins in form of supersaturated solid solution at 350 ℃, and experienced detectable Fe segregation at ITBs at 400 ℃, precipitation at 430 ℃ and complete recrystallization at 500 ℃. (c) Flow stress as a function of testing temperature indicates that NT $Al_{89.5}Fe_{5.5}Ti_{4.7}$ retains a flow stress of 1.7 GPa at 300 ℃.

C2. Design of super-strong and thermally stable NT Al-Ni-Ti alloys via solute synergy
(Yifan Zhang, Graduate Student, Nanoscale, 12(39), 2020)

To understand if Ti is an important solute to stabilize NT Al alloys in general, we explored solute synergy effect in another ternary Al alloy, Al-Ni-Ti. In this work, we demonstrate that minor additions of Ti solute (< 3at% Ti) to NT Al-Ni sputtered alloys significantly improves both the thermal stability and the strength as well. Micropillar compression tests (Fig. 16a-l) demonstrate a substantial increase of flow stress to 1.8 GPa with only 3at% Ti. The NT microstructure is stable up to 100 ^{o}C in Al-4.5Ni and up to 250 ^{o}C for Al-4.5Ni-3Ti, with a drop in hardness and breakdown of the solid solution at these temperatures leading to intermetallic formation, as demonstrated in the XRD scans in Fig. 12n.

DFT calculations were also conducted for this ternary NT Al alloy to determine the role Ti solute in the formation of the NT microstructure and the remarkable thermal stability. The excess energy change per surface atom with respect to reaction coordinate for surface trimer and heptamer were calculated and show in Fig. 17b-c, and demonstrate Ti raises the energy barrier for the migration of surface trimer and heptamers in Al-Ni and thus stabilize SFs in the Al-Ni system. Fig. 17d-f shows that Ni-Ti clusters near ITBs have the lowest formation energy comparing to the Ni-Ni and Ti-Ti pairs. Therefore Ti leads to a sluggish diffusion process for Ni in Al matrix and largely improved the thermal stability of SFs in Al-Ni system.

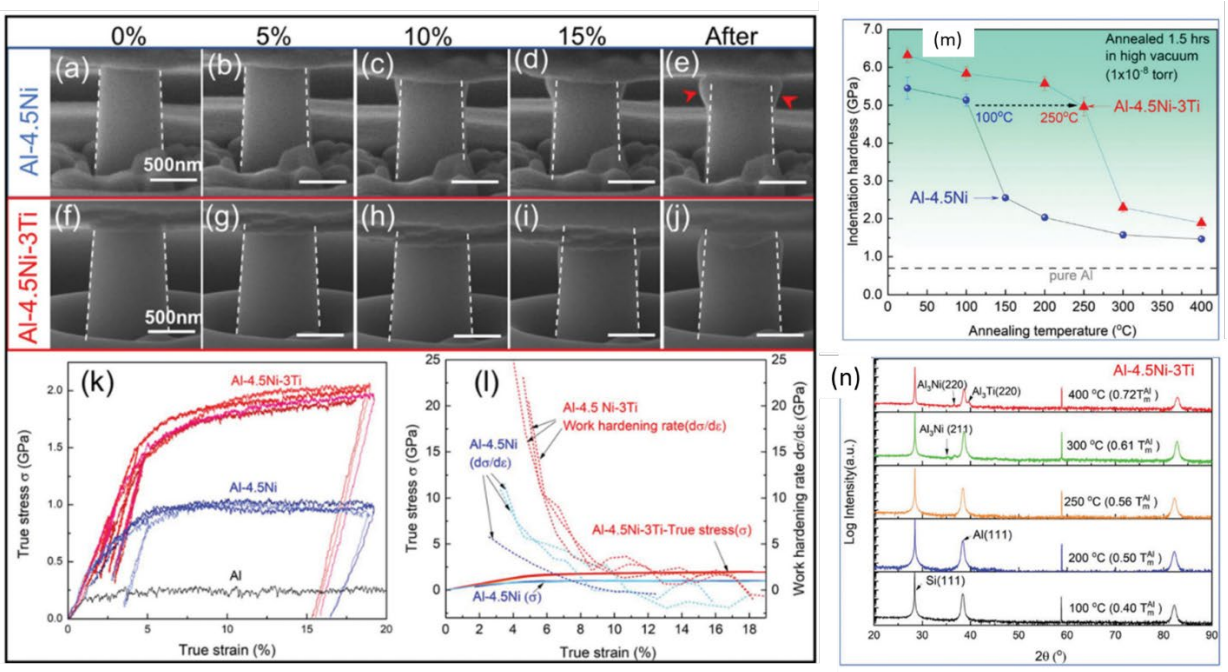

Figure 16. SEM snapshots showing the localized deformation on the pillar top of (a–e) deformed Al–4.5Ni and (f–j) Al–4.5Ni–3Ti pillar. (k) True stress–strain curves of Al, Al–4.5Ni, and Al–4.5Ni–3Ti alloys. (l) Work hardening rate (dσ/dε) and true stress (σ)of Al–4.5Ni and Al–4.5Ni–3Ti alloys vs. the true strain. (m) Hardnesses of Al–4.5 Ni and Al–4.5Ni–3Ti alloys annealed at different temperatures. (n) XRD scans of Al– 4.5Ni–3Ti alloy annealed at different temperatures under the high vacuum for 1.5 h.

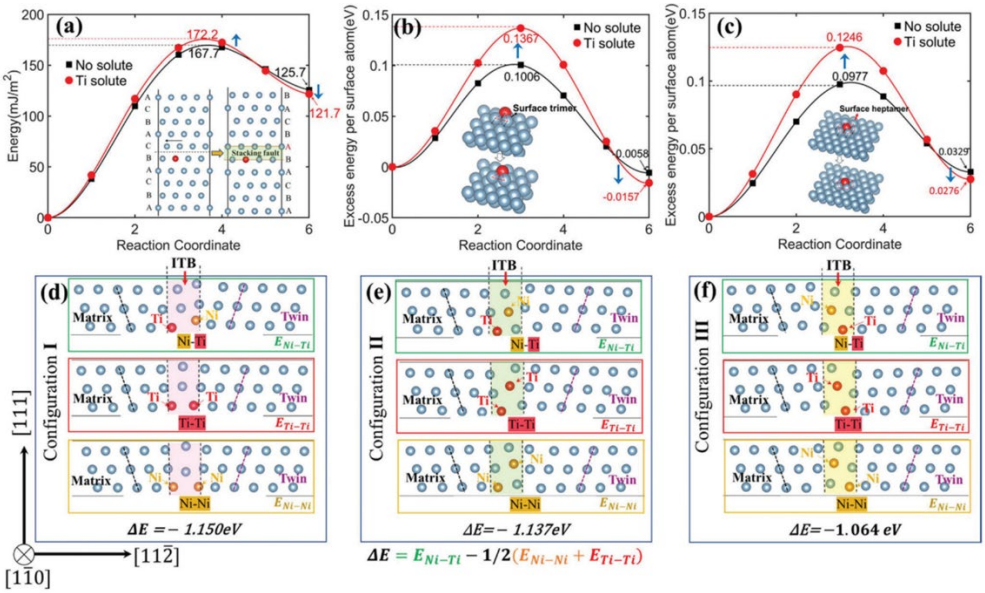

Figure 17. DFT calculation of solute impacts in Al alloy. (a) Slab models and calculated generalized stacking fault energy of Al with and without Ti solute as a function of the reaction coordinates. 0–6 corresponds to the FCC structure and stacking fault structures respectively. (b and c) The excess energy change per surface atom with respect to reaction coordinate for surface trimer and heptamer. (d–f) Three representative atomic configurations showing solute pairs near the ITBs with corresponding calculated energy difference.

C3. Thermal stability and grain coarsening resistance in NT Al–Co–Zr alloys (Nicholas Richter, Materials Science and Engineering: A, 862 Vol, 2023)

The thermal stability of NT Al-Co-Zr alloys was systematically studied through isochronal annealing to evaluate grain coarsening resistance and twin structure retention. The as-deposited films exhibited densely packed columnar grains with high densities of SFs and ITBs. Upon annealing at 300 °C, the microstructure remained largely unchanged, with retained twin networks and negligible grain growth (Fig. 18 a-d). At 400 °C, while some detwinning and boundary fragmentation occurred, the grain size remained below 100 nm, indicating a strong resistance to coarsening. STEM-EDS mapping revealed Co and Zr co-segregation at grain boundaries and interfaces (Fig. 19 a-d), leading to the formation of thermally stable Al_3Zr-like dispersoids. These nanoscale particles act as effective pinning centers, impeding grain boundary migration and stabilizing the twin network.

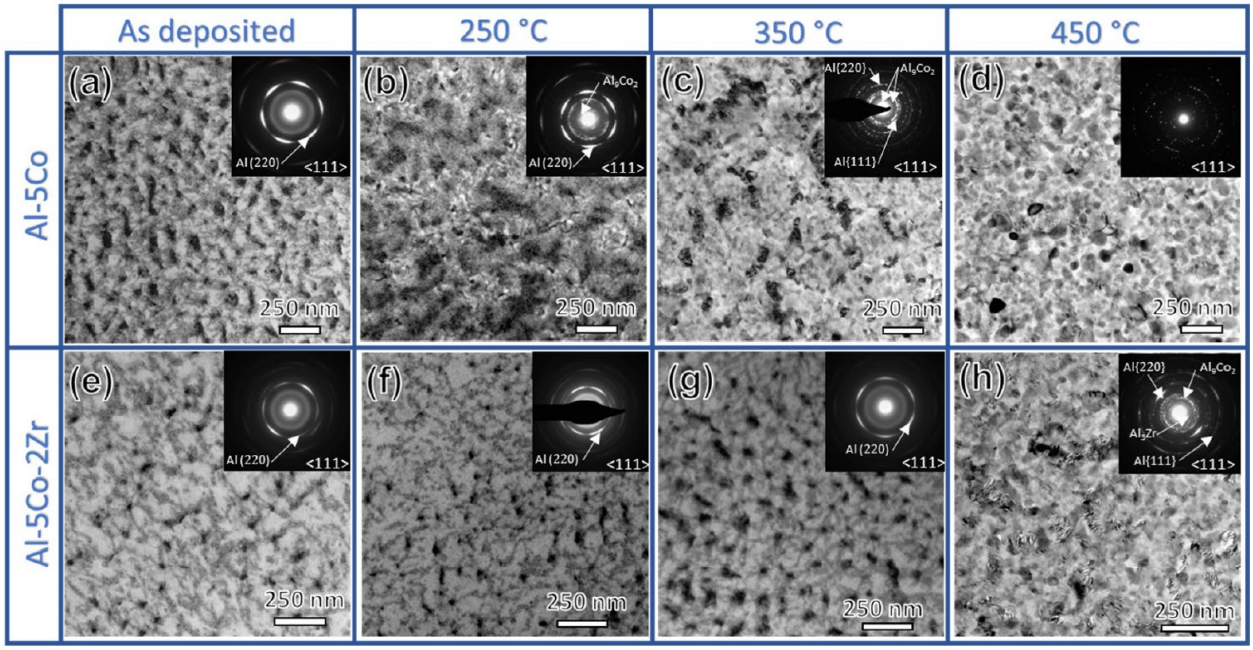

Fig. 18. (a–d) PV BFTEM images of Al-5Co and (e-h) Al-5Co-2Zr after vacuum annealing at indicated temperatures for 1.5 h.

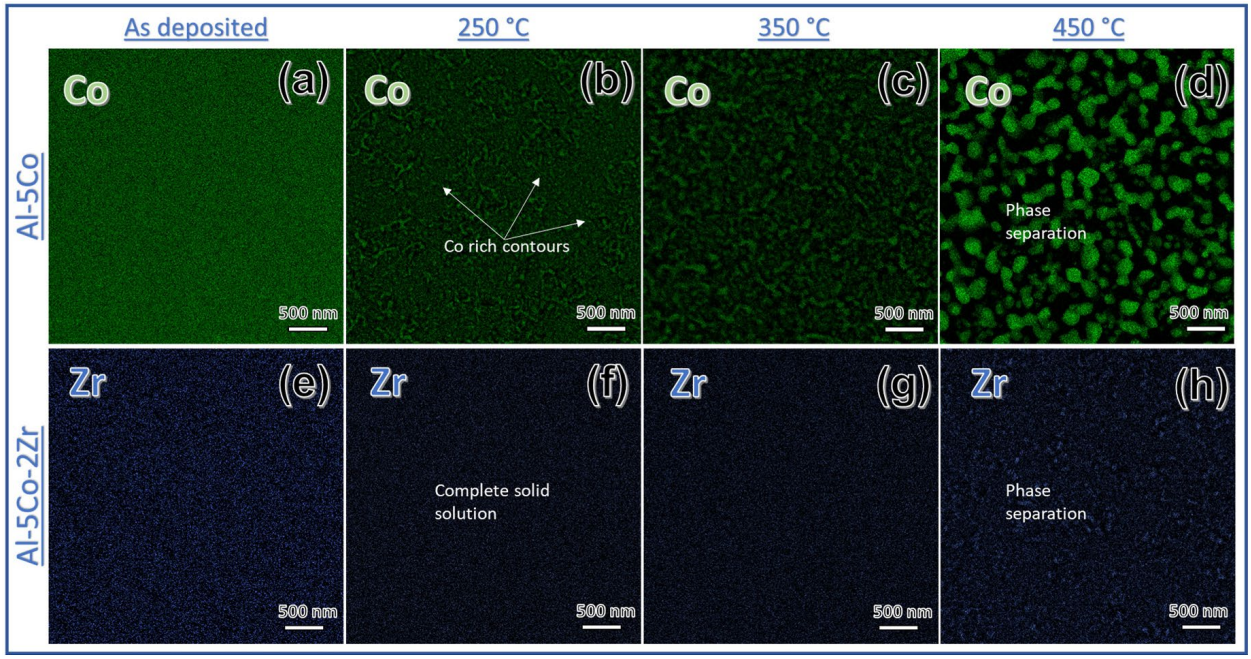

Fig. 19. (a-d) Co and Zr EDS maps of Al–5Co and (e-h) Al-5Co-2Zr after annealing at indicated temperatures.

Annealing at 500 °C triggered moderate grain growth and the onset of twin structure degradation, marked by blurred twin diffraction in SAED patterns and increased boundary

curvature. Despite this, the grain structure remained finer than that of pure or binary Al alloys. HRTEM and FFT analyses confirmed the persistence of residual SFs and partially coherent ITBs, suggesting that the twin structure degradation proceeded gradually. The superior thermal stability of Al-Co-Zr arises from the combined effects of high initial fault density and the Zener pinning effect provided by Al_3Zr dispersoids. Unlike NT Al-Ni alloys that rely solely on defect-driven stabilization, the ternary Al-Co-Zr system demonstrates enhanced microstructural stability via chemical and structural pathways.

Complementing this structural robustness, NT Al-Co-Zr alloys also retain remarkable mechanical performance after thermal exposure. Nanoindentation shows that the as-deposited hardness of ≈ 5.9 GPa (comparable to the strongest binary NT Al systems) drops by <4 % after 350 °C annealing and still exceeds 5 GPa, more than triple the hardness of commercial 7xxx Al alloys at ambient temperature. In-situ micropillar compression reveals a yield/flow stress of ≈ 1.1 GPa for the as-deposited film, with the pillars sustaining >15 % plastic strain via uniform barreling rather than shear localization (Fig. 20 b-e). Even after recrystallization at 450 °C, the flow stress remains ~0.5 GPa and the pillars continue to deform plastically without catastrophic fracture (Fig. 20k-r). This simultaneous retention of strength and ductility is attributed to three synergistic factors: (i) the high density of ITBs and 9R phase that serve as potent barriers to dislocation glide and promote work-hardening; (ii) Zr-rich Al_3Zr dispersoids that pin boundaries and impede detwinning, thereby preserving the load-bearing twin network; and (iii) solute drag from slow-diffusing Zr, which stabilizes Co at ITBs and suppresses coarse intermetallic precipitation. Together, these mechanisms allow NT Al-Co-Zr alloys to outperform both binary NT Al-Co and conventional nanocrystalline Al alloys in high-temperature strength–ductility retention, making them strong candidates for lightweight components operating up to ~0.75 melting temperature.

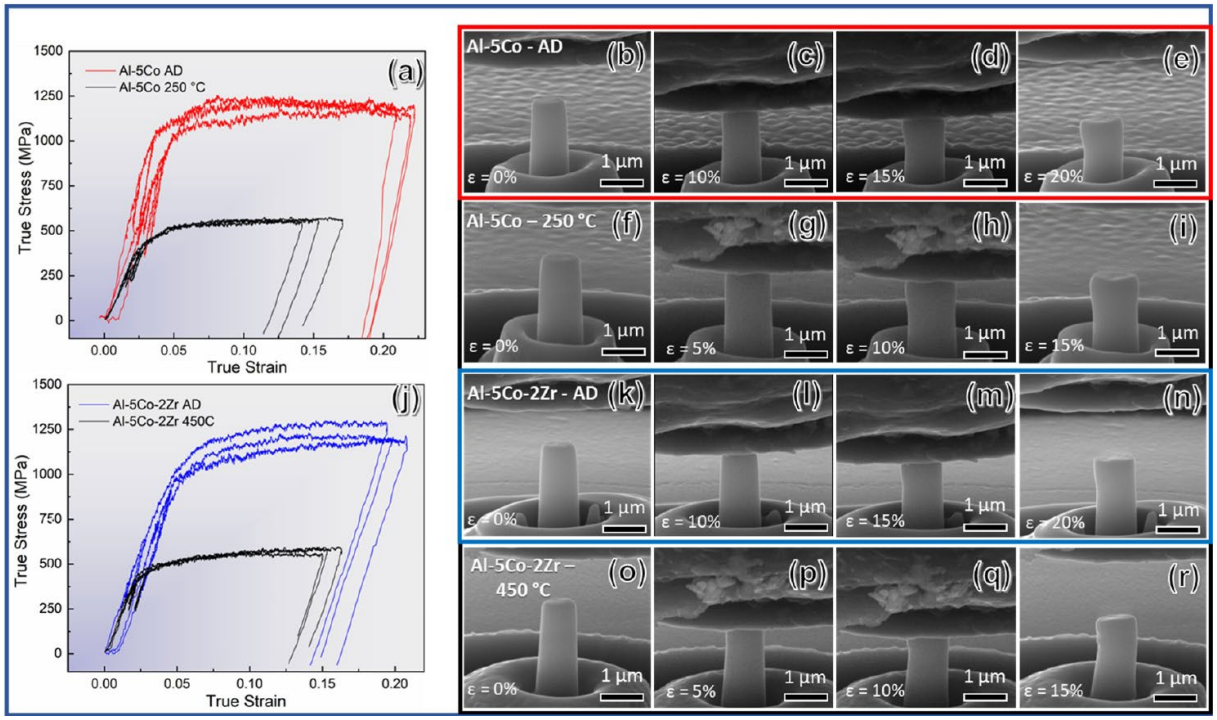

Fig. 20. n-situ micropillar compression of as-deposited and annealed Al-5Co and Al-5Co-2Zr with NT structures. (a) True stress–strain curves for Al-5Co before and after 250 °C annealing. (b-e) SEM snapshots of as-deposited and (f-i) annealed Al-5Co during compression. (j) Stress-strain curves for Al-5Co-2Zr before and after 450 °C annealing. (k-n) SEM snapshots of as-deposited and (o-r) annealed Al-5Co-2Zr at various strain levels. Supplementary videos available.

II. A list of papers published, in press, or submitted

1. X.Y. Sheng, Z.X. Shang, Y.F. Zhang, K. Xu, N.A. Richter, A.Y. Shang, H. Wang, and X. Zhang, Ultra-high strength, deformable nanocrystalline Al-Pd alloys, International Journal of Plasticity 189 (2025) 104330.

Acknowledgement: This work is supported by the Department of Energy-Office of Basic Energy Sciences (grant number: DE-SC0016337).

2. XY Sheng, Z Shang, AY Shang, H Wang, X Zhang, Grain boundary and twin boundary solute segregations in nanocrystalline Al-Mg alloy, Scripta Materialia, 245 (2024) 116053.

Acknowledgement: This work is supported by the Department of Energy-Office of Basic Energy Sciences (grant number: DE-SC0016337).

3. Nicholas A Richter, YiFan Zhang, Mingyu Gong, Tongjun Niu, Bo Yang, Sichuang Xue, Jian Wang, Haiyan Wang, Xinghang Zhang, Solute synergy induced thermal stability of high-strength

nanotwinned Al-Co-Zr alloys, **Materials Science and Engineering: A**, 862 (2023) 144477.

Acknowledgement: This work is supported by the Department of Energy-Office of Basic Energy Sciences (grant number: DE-SC0016337).

4. XY Sheng, NA Richter, AY Shang, H Wang, X Zhang, Twin density and twin thickness evolution in sputtered Al–Mg alloys, **Journal of Applied Physics,** 133 (2023) 205301.

Acknowledgement: This work is supported by the Department of Energy – Basic Energy Science (DOE Award number:DE-SC0016337).

5. Nicholas Allen Richter, Xuanyu Sheng, Bo Yang, Benjamin Thomas Stegman, Haiyan Wang, Xinghang Zhang, Assessing Strain Rate Sensitivity of Nanotwinned Al–Zr Alloys through Nanoindentation, **Crystals,** 13 (2023) 276.

Acknowledgement: This work is supported by the Department of Energy – Basic Energy Science (DOE Award number:DE-SC0016337).

6. Yifan Zhang, Tongjun Niu, Nicholas A Richter, Tianyi Sun, Nan Li, Haiyan Wang, Xinghang Zhang, Tribological behaviors of nanotwinned Al alloys, **Applied Surface Science,** 600 (2022) 154108.

Acknowledgement: This work is supported by the Department of Energy – Basic Energy Science (DOE Award number:DE-SC0016337).

7. NA Richter, M Gong, YF Zhang, T Niu, B Yang, J Wang, H Wang, X Zhang, Exploring the deformation behavior of nanotwinned Al–Zr alloy via *in situ* compression, **Journal of Applied Physics** 132 (2022), 065104

Acknowledgement: This work is supported by the Department of Energy – Basic Energy Science (DOE Award number:DE-SC0016337).

8. S. Xue, Y. Zhang, Q. Li, J. Ding, H. Wang and X. Zhang, Tailoring the formation of twins in Al by introducing epitaxial layer interfaces, **Scripta Materialia,** 192 (2021), 1-6.

Acknowledgement: This work is supported by the Department of Energy-Office of Basic Energy Sciences (grant number: DE-SC0016337).

9. N. Richter, Y. Zhang, D. Xie, R. Su, Q. Li, S. Xu, T. Niu, J. Wang, H. Wang and X Zhang, Microstructural evolution of nanotwinned Al-Zr alloy with significant 9R phase, **Materials Research Letters,** 9(2) (2021) 91-98.

Acknowledgement: This work is supported by the Department of Energy-Office of Basic Energy Sciences (grant number: DE-SC0016337).

10. Q. Li, Z. Shang, X. Sun, C. Fan, R. Su, N. Richter, Z. Fan, Y. Shang, S. Xue, H. Wang and X. Zhang, High-strength and tunable plasticity in sputtered Al–Cr alloys with multistage phase transformations, **International Journal of Plasticity,** 137 (2021) 102915.

Acknowledgement: This work is supported by the Department of Energy-Office of Basic Energy Sciences (grant number: DE-SC0016337).

11. Mingyu Gong, Wenqian Wu, Dongyue Xie, Nicholas A Richter, Qiang Li, Yifan Zhang, Sichuang Xue, Xinghang Zhang, Jian Wang, First-principles calculations for understanding microstructures and mechanical properties of co-sputtered Al alloys, **Nanoscale, 13**, (2021) 14987-15001.

Acknowledgement: This work is supported by the Department of Energy – Basic Energy Science (DOE Award number:DE-SC0016337).

12. Q. Li, S. Xue, Y. Zhang, X. Sun, H. Wang, X. Zhang, Plastic anisotropy and tension-compression asymmetry in nanotwinned Al–Fe alloys: An in-situ micromechanical investigation, **International Journal of Plasticity**, 132 (2020) 102760.

Acknowledgement: This work is supported by the Department of Energy-Office of Basic Energy Sciences (grant number: DE-SC0016337).

13. Y. Zhang, Q. Li, M. Gong, S. Xue, J. Ding, J. Li, J. Cho, T. Niu, R. Su, N. Richter, H. Wang, J. Wang, and X. Zhang, Deformation behavior and phase transformation of nanotwinned Al/Ti multilayers, **Applied Surface Science**, 527 (2020) 146776.
Acknowledgement: This work is supported by the Department of Energy-Office of Basic Energy Sciences (grant number: DE-SC0016337).

14. Q. Li, D. Xie, Z. Shang, X. Sun, J. Cho, Y. Zhang, S. Xue, H. Wang, J. Wang and X. Zhang, Coupled solute effects enable anomalous high-temperature strength and stability in nanotwinned Al alloys, **Acta Materialia**, 200 (2020), 378-388.
Acknowledgement: This work is supported by the Department of Energy-Office of Basic Energy Sciences (grant number: DE-SC0016337).

15. Y. Zhang, R. Su, D. Xie, T. Niu, S. Xue, Q. Li, J. Ding, N. Richter, J. Wang, H. Wang and X. Zhang, Design of super-strong and thermally stable nanotwinned Al alloys via solute synergy, **Nanoscale,** 12(39) (2020) 20491-20505.

Acknowledgement: This work is supported by the Department of Energy-Office of Basic Energy Sciences (grant number: DE-SC0016337).

16. Q. Li, S. Xue, P. Price, X. Sun, J. Ding, Z. Shang, Z. Fan, H. Wang, Y. Zhang, Y. Chen, H. Wang, K. Hattar, and X. Zhang, Hierarchical nanotwins in single-crystal-like nickel with high strength and corrosion resistance produced via a hybrid technique, **Nanoscale**, 12 (2020) 1356.

Acknowledgement: This work is supported by the Department of Energy-Office of Basic Energy Sciences (grant number: DE-SC0016337).

III. Patents

1. Q. Li, S. Xue, Y. Zhang, and X. Zhang. (2020). Aluminum alloy coatings with high strength and thermal stability and method of making the same. Application #: 17106964. US Patent Office.
2. Q. Li, X. Zhang, H. Wang and J. Ding. (2020). High-strength single-crystal like nanotwinned nickel coatings and methods of making the same. WO/2020/005949. US Patent Office.
3. Q. Li; X. Zhang; Y. Zhang; S. Xue; H. Wang, "METHODS OF INCREASING STRENGTH AND THERMAL STABILITY OF ALUMINUM ALLOY COATINGS AND ALUMINUM COATINGS MADE THEREFROM", USPTO Provisional Patent filing: 62967923, 2020.

IV. A list of people working on the project

Name	Title	Percentage of support
Xinghang Zhang	PI	1%
Nicholas A. Richter	Ph.D. student (Now at Oak Ridge National Lab, postdoc)	100%
Xuanyu Sheng	Ph.D. student (Now at LAM Research)	100%
Jian Wang	Co-PI	1%
Mingyu Gong	Post-doctoral fellow	50%
Dongyue Xie	Ph.D. Student (Postdoc at Los Alamos National Lab)	50%